MBoC | BRIEF REPORT

# Tubulin isoform composition tunes microtubule dynamics

Annapurna Vemu[a], Joseph Atherton[b], Jeffrey O. Spector[a], Carolyn A. Moores[b], and Antonina Roll-Mecak[a,c,*]

[a]Cell Biology and Biophysics Unit, National Institute of Neurological Disorders and Stroke, and [c]Biophysics Center, National Heart, Lung and Blood Institute, Bethesda, MD 20892; [b]Institute of Structural and Molecular Biology, Department of Biological Sciences, Birkbeck College, University of London, London WC1E 7HX, United Kingdom

**ABSTRACT** **Microtubules polymerize and depolymerize stochastically, a behavior essential for cell division, motility, and differentiation. While many studies advanced our understanding of how microtubule-associated proteins tune microtubule dynamics in trans, we have yet to understand how tubulin genetic diversity regulates microtubule functions. The majority of in vitro dynamics studies are performed with tubulin purified from brain tissue. This preparation is not representative of tubulin found in many cell types. Here we report the 4.2-Å cryo-electron microscopy (cryo-EM) structure and in vitro dynamics parameters of α1B/βI+βIVb microtubules assembled from tubulin purified from a human embryonic kidney cell line with isoform composition characteristic of fibroblasts and many immortalized cell lines. We find that these microtubules grow faster and transition to depolymerization less frequently compared with brain microtubules. Cryo-EM reveals that the dynamic ends of α1B/βI+βIVb microtubules are less tapered and that these tubulin heterodimers display lower curvatures. Interestingly, analysis of EB1 distributions at dynamic ends suggests no differences in GTP cap sizes. Last, we show that the addition of recombinant α1A/βIII tubulin, a neuronal isotype overexpressed in many tumors, proportionally tunes the dynamics of α1B/βI+βIVb microtubules. Our study is an important step toward understanding how tubulin isoform composition tunes microtubule dynamics.**

**Monitoring Editor**
Laurent Blanchoin
CEA Grenoble

Received: Feb 27, 2017
Revised: Sep 25, 2017
Accepted: Oct 3, 2017

## INTRODUCTION

Microtubules are essential dynamic polymers that stochastically switch between polymerization and depolymerization, a behavior known as dynamic instability (Mitchison and Kirschner, 1984; Horio and Hotani, 1986). Dynamic instability is essential for basic cellular processes such as cell division, motility, and differentiation. The building block of the microtubule is the α/β-tubulin heterodimer. Cells use a diverse repertoire of tubulin dimers to build complex structures with diverse architectures and dynamics to perform these basic cellular functions. Eukaryotes have multiple tubulin isotypes; humans have eight α- and eight β-tubulin isotypes (Redeker, 2010). While some tubulin isoforms are ubiquitously expressed, others are only found in specialized cells such as sperm, neurons, and platelets (Denoulet *et al.*, 1986; Villasante *et al.*, 1986; Wang *et al.*, 1986; Leandro-García *et al.*, 2010). In vivo studies have shown that tubulin isoforms are not functionally interchangeable, suggestive of differential microtubule associate protein (MAPs) recruitment by tubulin isoforms or changes in intrinsic polymer properties (Hoyle and Raff, 1990; Saillour *et al.*, 2014). Tubulin is further functionalized through chemically diverse posttranslational modifications that include glutamylation, glycylation, acetylation, phosphorylation, and amination (Yu *et al.*, 2015).

The majority of in vitro assays are performed with tubulin purified from brain tissue through repeated cycles of polymerization and depolymerization (Weisenberg *et al.*, 1968). While cost-effective, this procedure generates tubulin that is highly heterogeneous, consisting of multiple tubulin isotypes that have chemically diverse and abundant posttranslational modifications (Banerjee *et al.*, 1988; Zambito

This article was published online ahead of print in MBoC in Press (http://www.molbiolcell.org/cgi/doi/10.1091/mbc.E17-02-0124) on October 11, 2017.

Author contributions: A.V. purified tubulin, A.V. and J.O.S. performed and analyzed dynamics assays, and J.A. determined EM structure. All authors interpreted data. A.R.-M., A.V., J.A., and C.A.M. wrote the manuscript. A.R.-M. conceived and supervised the project.

*Address correspondence to: Antonina Roll-Mecak (Antonina@mail.nih.gov).

Abbreciations used: AMPPNP, 5′ adenylyl-β,γ-imidodiphosphate; cryo-EM, cryo-electron microscopy; GMPCPP, guanylyl-(α,β)-methylene-diphosphonate; PDB, Protein Data Bank.



Supplemental Material can be found at:
http://www.molbiolcell.org/content/suppl/2017/10/09/mbc.E17-02-0124v1.DC1

*et al.*, 2002). Most importantly, the composition of tubulin isotypes and tubulin posttranslational modifications in these preparations is not representative of that found in most cell types as well as many of the cell lines routinely used in cell biological investigations. Classic studies have reported the characterization of tubulin with less complex compositions purified through polymerization/depolymerization cycles from chicken erythrocytes (Murphy and Wallis, 1983, 1986) and HeLa cells (Newton *et al.*, 2002). A recently introduced affinity purification approach finally enabled the isolation of biochemical amounts of tubulin from various tissues and cell lines (Widlund *et al.*, 2012) that together with recent advances in the expression and purification of pure single isoform human tubulin open a new chapter in the investigation of the biophysical correlates between tubulin sequence, structure, and dynamics (Minoura *et al.*, 2013; Vemu *et al.*, 2016).

Here we purify tubulin from a human embryonic kidney (tsA201) cell line and report its 4.2-Å cryo-electron microscopy (cryo-EM) structure and dynamic parameters. Tubulin purified from this cell line consists predominantly of one α-tubulin isoform, α1B, and two β-tubulin isoforms, βI and βIVb. This β-tubulin composition is characteristic for fibroblasts (Lopata and Cleveland, 1987) as well as cancer cell lines (Rao *et al.*, 2001; Hiser *et al.*, 2006) commonly used for cell biological investigations. In vitro dynamic assays show that these microtubules grow faster and undergo catastrophe less frequently than brain microtubules and cryo-EM reveals structural differences at their dynamic ends. Moreover, we show that microtubule dynamic parameters vary proportionally with the ratio between this nonneuronal tubulin and a recombinantly produced neuronal tubulin isoform that has different dynamic properties. Thus, differential use of tubulin isoforms can have pronounced effects on microtubule structure and dynamics.

## RESULTS AND DISCUSSION

### In vitro dynamics of human unmodified α1B/βI+βIVb tubulin

We purified tubulin from mouse brain and a human embryonic kidney cell line (tsA 201) using a modified tumor overexpressed gene (TOG)-affinity method (Widlund *et al.*, 2012; Vemu *et al.*, 2014) (see *Materials and Methods*) to obtain the purity required for reproducible in vitro dynamics assays. Mass spectrometric analysis shows that tubulin isolated from this cell line contains predominantly unmodified α–tubulin, α1B, and two β-tubulin isoforms, βI and βIVb (Figure 1). To allow a side-by-side comparison, we also purified mouse brain tubulin using the same TOG-based purification procedure (see *Materials and Methods*). Mass spectrometric analysis shows its high level of heterogeneity with more than 30 different separate species consisting of varied α- and β-tubulin isoforms and abundant posttranslational modifications, especially glutamylation.

To examine the dynamics of α1B/βI+βIVb tubulin, we performed label-free in vitro dynamic assays using darkfield microscopy (Figure 2). To quantify dynamic parameters, we generated kymographs from time-lapse images of dynamic microtubules (Figure 2A). We find the plus-end growth rates for α1B/βI+βIVb microtubules are approximately twofold faster than brain microtubules (Figure 2D). Consistent with this, the plus-end on-rate is 3.7 dimers $s^{-1}$ $\mu M^{-1}$ compared with 2.0 dimers $s^{-1}$ $\mu M^{-1}$ for brain tubulin (Figure 2C). The plus-end catastrophe frequency (the transition from growth to shrinkage) is approximately twofold lower than that of brain microtubules (Figure 2D). Earlier studies reported HeLa microtubules composed mainly of βI+βIVb tubulin and an unknown α-tubulin composition undergo catastrophe less than brain microtubules, in agreement with our observations (Newton *et al.*, 2002). The minus-end growth rates and catastrophe frequencies for α1B/βI+βIVb microtubules are statistically indistinguishable from brain microtubules (Figure 2E). The dynamic parameters observed for α1B/βI+βIVb microtubules are reproducible across multiple purifications from different tsA201 cell growths (Supplemental Figure S1A). Thus, unmodified α1B/βI+βIVb microtubules are more stable and reach longer mean lengths than heterogeneous brain microtubules. The α1B/βI+βIVb microtubules also undergo catastrophe less frequently than recombinant single isoform α1A/βIII microtubules (Vemu *et al.*, 2016). The threefold increase in mean microtubule length from 3.9 ± 0.3 µm to 10.7 ± 0.6 µm for α1B/βI+βIVb microtubules is achieved mainly through a combination of catastrophe suppression and polymerization enhancement (Figure 2D). Interestingly, the α1B/βI+βIVb microtubules grow threefold faster than the *Saccharomyces cerevisiae* microtubules but have significantly lower catastrophe frequencies (Podolski *et al.*, 2014).

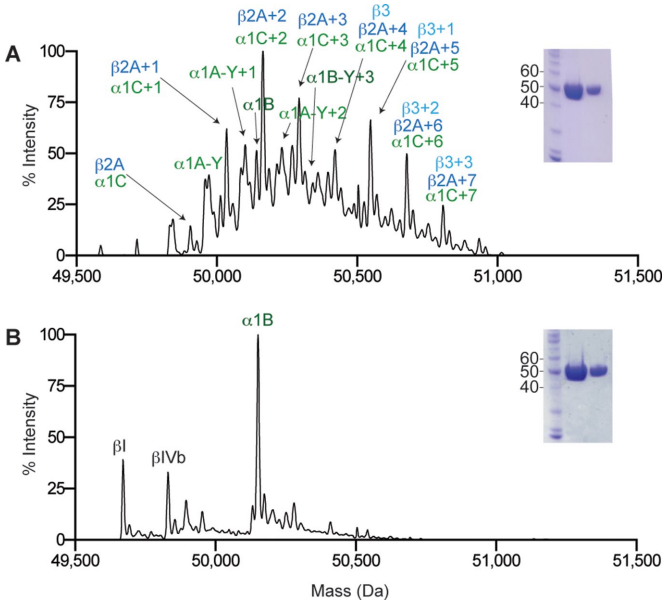


**FIGURE 1:** Isoform composition and purity of tubulin isolated from brain tissue and tsA201 cells using the TOG affinity method. (A) Mass spectra and SDS–polyacrylamide gel (inset) of tubulin isolated from mouse brain. Number of posttranslationally added glutamates is indicated for the glutamylated species. (B) Mass spectra and SDS–polyacrylamide gel (inset) tubulin isolated from tsA201 cells (see *Materials and Methods*).

Darkfield imaging allows acquisition at high frame rates that enables the determination of depolymerization rates with high accuracy. These measurements show that α1B/βI+βIVb microtubules depolymerize 33% faster than brain microtubules (Figure 2B). The depolymerization rate of α1B/βI+βIVb microtubules is also faster than that of neuronal α1A/βIII recombinant microtubules (38.9 ± 2.3 µm/min and 30.5 ± 1.3 µm/min for α1B/βI+βIVb and α1A/βIII microtubules, respectively [Vemu *et al.*, 2016]). It will be important to establish whether microtubules with different isoform compositions can generate different end depolymerization forces that could be harnessed to move cargo in the cell, such as chromosomes during cell division (Grishchuk *et al.*, 2005)

### 4.2 Å cryo-EM structure of unmodified α1B/βI+βIVb microtubules

To further gain insight into its assembly properties, we determined the structure of α1B/βI+βIVb microtubules in the presence of the nonhydrolyzable GTP-analogue guanylyl-(α,β)-methylene-diphosphonate (GMPCPP) using cryoelectron microscopy and single-particle reconstruction (Figure 3A). The overall resolution of the reconstruction is ~4.2 Å (Supplemental Figure S2A, gold-standard

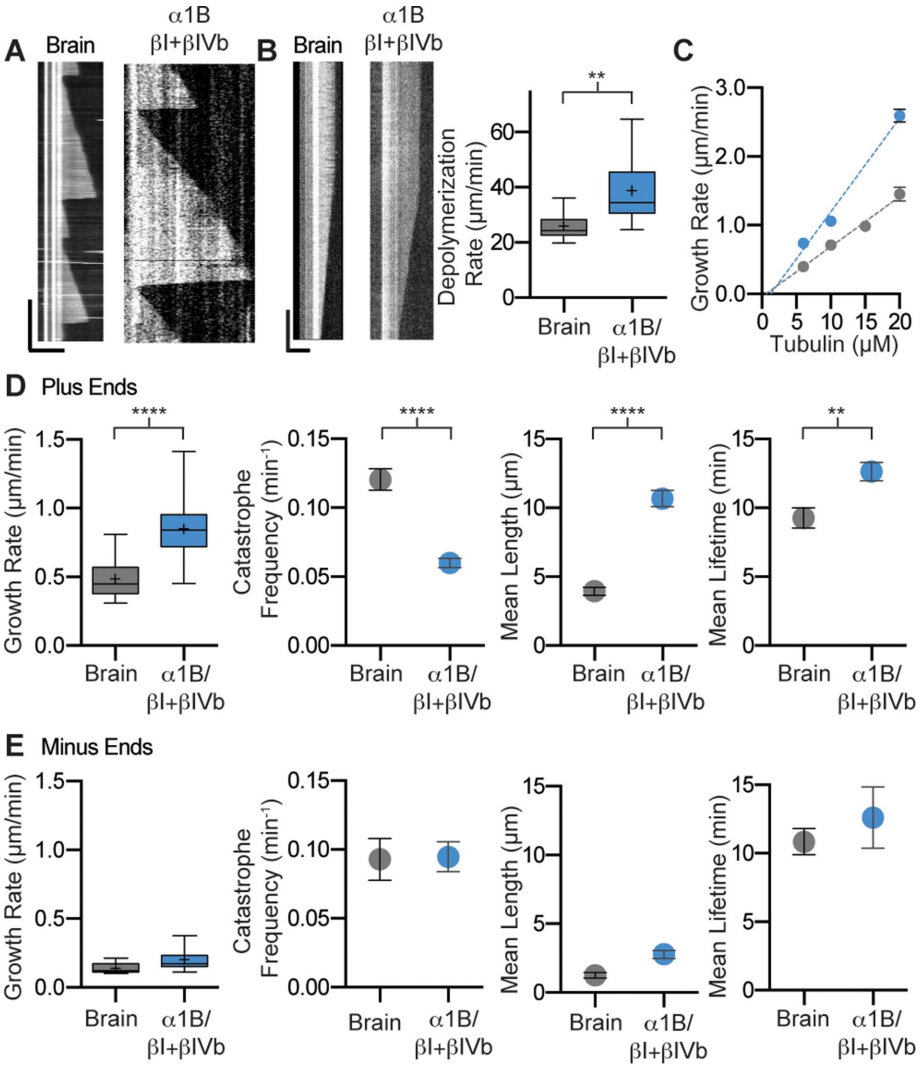


**FIGURE 2:** Dynamics of brain and α1B/βI+βIVb microtubules. (A) Kymographs showing typical microtubule growth for brain and α1B/βI+βIVb tubulin at 6 μM. Horizontal and vertical scale bars, 5 μm and 5 min, respectively. (B) Left: kymographs showing a typical depolymerization event for brain and α1B/βI+βIVb microtubules. Horizontal and vertical scale bars, 5 μm and 2 s, respectively. Right: Tukey plot showing plus-end depolymerization rates at 6 μM tubulin; $n = 12$ and 27 events for brain and α1B/βI+βIVb microtubules, respectively. (C) Plus-end growth rates as a function of varying tubulin concentration for brain (gray) and α1B/βI+βIVb microtubules (blue). (D) Plus-end dynamics of brain (gray) and α1B/βI+βIVb (blue) microtubules at 6 μM tubulin. From left to right: box-whisker plot (whiskers indicate minimum and maximum) showing plus-end growth rates for brain and α1B/βI+βIVb microtubules; $n = 38$ and 191 events for brain and α1B/βI+βIVb tubulin, respectively. Plus-end catastrophe frequencies; $n = 20$ and 69 microtubules for brain and α1B/βI+βIVb tubulin, respectively. Plus-end microtubule mean lengths; $n = 49$ and 102 events for brain and α1B/βI+βIVb tubulin, respectively. Plus-end microtubule mean lifetimes; $n = 49$ and 102 events for brain and α1B/βI+βIVb tubulin, respectively. (E) Minus-end dynamics of brain and α1B/βI+βIVb tubulin at 6 μM tubulin. From left to right: box-whisker plot (whiskers indicate minimum and maximum) showing minus-end growth rates for brain and α1B/βI+βIVb tubulin; $n = 12$ and 84 events for brain and α1B/βI+βIVb tubulin, respectively. Minus-end catastrophe frequencies; $n = 10$ and 33 microtubules for brain and α1B/βI+βIVb tubulin, respectively. Minus-end microtubule mean lengths; $n = 9$ and 10 events for brain and α1B/βI+βIVb, respectively. Minus-end microtubule mean lifetimes; $n = 9$ and 10 events for brain and α1B/βI+βIVb, respectively. ** and ****, $p$ values < 0.01 and < 0.0001, respectively, determined by unpaired $t$ test.

noise-substitution test; Fourier shell correlation 0.143 criterion [Chen *et al.*, 2013]); however, assessment of local resolution suggests that much of the tubulin falls within a higher resolution range (~3.5 Å in more buried regions to ~4.5 Å in the most surface exposed regions; Supplemental Figure S2). At this resolution the pitch of helices, β-strand separation and side-chain densities were apparent and occupancy of nucleotide triphosphate could be seen at both the E- and N-site in βI+βIVb and α1B-tubulin, respectively (Figure 3, A and B). The structures of microtubules formed from α1B/βI+βIVb and brain tubulin (previously determined, PDB, 3JAT) are similar. No significant differences were detected at either lateral or longitudinal interfaces between tubulin dimers at this resolution. The dimer repeat distance in GMPCPP α1B/βI+βIVb microtubules (83.4 Å ± 0.1 Å) was only slightly longer than that in GMPCPP brain microtubules (83.1 ± 0.0 Å), consistent with the presence of an "extended" lattice in microtubules polymerized with this nucleotide analogue (Alushin *et al.*, 2014; Zhang *et al.*, 2015). Despite the lower heterogeneity of this sample compared with brain tubulin (Figure 1) the C-terminal tails and acetylation loop are still unresolved in our reconstruction presumably due to the flexibility of these regions in the absence of effectors as seen in previous reconstructions of both heterogeneous brain microtubules and single-isoform recombinant microtubules (Garnham *et al.*, 2015; Zhang *et al.*, 2015; Vemu *et al.*, 2016).

Dynamic microtubules polymerized with GTP (see *Materials and Methods*) showed similar protofilament distributions for both brain microtubules (mouse purified through the TOG affinity procedure or commercial bovine from Cytoskeleton) and α1B/βI + βIVb microtubules, with the large majority containing 14 protofilaments and nearly all remaining microtubules containing 13 protofilaments (Supplemental Figure S2, C and D). The ends of dynamic growing microtubules transition from the straight lattice characteristic of the stable polymer to a curved and tapered region where protofilaments are missing, as has been previously described (Mandelkow *et al.*, 1991; Chrétien *et al.*, 1995). This feature was clear in micrographs of polymerizing brain and α1B/βI+βIVb tubulin (Figure 3C). Measurements of the tapered region for dynamic α1B/βI+βIVb and brain microtubules revealed a wide distribution from very short (<10 nm) to rare but very long (>100 nm) end regions for both (Figure 3D). Although the distributions show a large degree of overlap, α1B/βI+βIVb microtubule tapered ends were shorter than those of brain microtubule populations (Figure 3D; 30.3 ± 3.3 nm vs. 53.5 ± 7.3 nm for α1B/βI+βIVb and brain [mouse TOG tubulin], respectively). This difference was present regardless of the method used to purify the brain tubulin: commercial bovine brain microtubules (Cytoskeleton) showed a distribution similar to that of

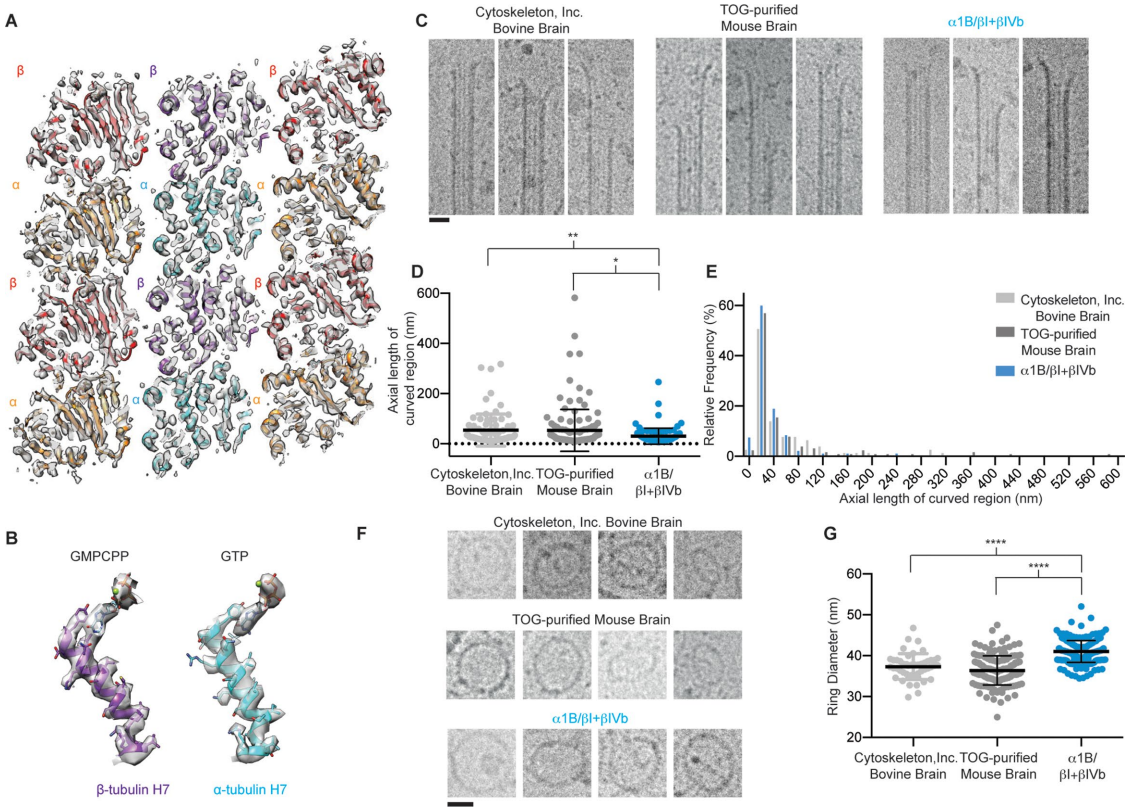


**FIGURE 3:** Cryoelectron microscopy of α1B/βI+βIVb microtubules. (A) Cross-section of the cryo-EM map (gray density) and model of GMPCPP human α1B/βI+βIVb microtubules (three protofilaments shown). A central protofilament (Pf2) makes lateral contacts with adjacent protofilaments (Pf1 and Pf3); α-tubulin, orange, β-tubulin, red (Pf1, Pf3); α-tubulin, cyan; β-tubulin, purple (Pf2). (B) β-Tubulin helix H7 and GMPCPP (left, purple) and α-tubulin helix H7 and GTP (right, cyan) and their corresponding experimental densities (gray density). (C) Gallery of polymerizing brain (bovine [Cytoskeleton] and mouse, TOG-affinity purified) and α1B/βI+βIVb microtubule ends. Similar architectures are observed, including short and long taper/curved region lengths. Scale bar: 20 nm. (D) Quantification of the length of the curved/tapered region for brain (bovine [Cytoskeleton] and mouse, TOG-affinity purified) and α1B/βI+βIVb microtubule ends; $n = 79$, 130, and 95 for mouse brain, bovine brain, and α1B/βI+βIVb microtubule ends, respectively. ** and *$p$ value $< 0.01$ or $< 0.05$, respectively, as determined by the Mann-Whitney test. (E) Histogram showing curved/tapered region length frequency of α1B/βI+βIVb microtubule ends. (F) Gallery of tubulin rings in dynamic preparations of commercial bovine brain (Cytoskeleton) microtubules (top), TOG-affinity purified mouse brain, microtubules (middle), and α1B/βI+βIVb microtubules (bottom) showing rings of different diameters and orientations. Scale bar: 20 nm. (G) Quantification of maximum ring diameter from brain (bovine [Cytoskeleton] and mouse, TOG-affinity purified) and α1B/βI+βIVb dynamic microtubule preparations; $n = 48$, 151, and 240 for bovine brain, mouse brain, and α1B/βI+βIVb. **** $p$ value $< 0.0001$ determined by the Mann-Whitney test.

microtubules assembled from TOG affinity purified mouse brain tubulin (Figure 3D; 53.5 ± 7.3 nm vs. 54.4 ± 7.2 nm). This commercial tubulin also showed similar dynamic parameters to the brain tubulin purified using the TOG affinity approach (Supplemental Figure S1B). In addition, the variance of the tapered ends lengths was lower for α1B/βI+βIVb microtubules, with the frequency distribution of α1B/βI+βIVb microtubules more skewed toward shorter tapered ends and longer ends for brain microtubules (Figure 3E). The less tapered end architecture of α1B/βI+βIVb microtubules could reflect a higher probability of successful incorporation of the more homogeneous α1B/βI+βIVb dimers in the microtubule lattice compared with brain tubulin or faster closure of the tapered structures into a complete lattice. The highly heterogeneous mixture of the brain dimers could lead to heterogeneities in the lattice and the pause in growth of some protofilaments, thus the more varied and extreme tapered structures. We note that these measurements were collected from tubulin polymerized at 5 mg/ml in all cases. Future studies examining taper lengths at a range of tubulin concentrations—which yield different growth rates for each tubulin (Figure 2C)—will more firmly establish the link between the dynamic and structural properties of the ends of these microtubules.

In dynamic microtubule preparations viewed by cryo-EM, a proportion of tubulin "peeling" from depolymerizing microtubule ends closes into rings containing longitudinally associated, curved tubulin dimers (Mandelkow *et al.*, 1991). We observed tubulin rings in micrographs of dynamic α1B/βI+βIVb and brain microtubule preparations (Figure 3F). Even though shapes, sizes and orientations of rings in two-dimensional cryo-EM images projections vary, the longest wall-to-wall distance in the rings provides a measure of overall protofilament curvature. Ring diameters for these sets of dynamic microtubules were measured. These showed that α1B/βI+βIVb rings are significantly larger on average (41.0 ± 0.2 nm) than those formed by brain tubulin (36.4 ± 0.3 nm and 37.3 ± 0.5 nm for TOG purified and commercial brain tubulin,

respectively) (Figure 3G). Thus, the average tubulin curvature per dimer length (8.2 nm) is 22.8° and 25.8° for α1B/βI+βIVb and brain tubulin, respectively (Figure 3G). Tubulin dimers need to straighten on incorporation into the microtubule lattice (VanBuren *et al.*, 2002; Wang and Nogales, 2005; Rice *et al.*, 2008). One interpretation of our data is that the energy penalty for straightening the α1B/βI+βIVb dimers during microtubule incorporation is lower, consistent with their higher polymerization rate. More work on tubulin from different sources will be required to establish this connection.

### Similar EB1 distributions on α1B/βI+βIVb and brain microtubules suggest similar cap sizes

Polymerizing microtubules are protected from depolymerization by a GTP cap at their ends generated by a lag between the GTP hydrolysis rate of the incorporated tubulin and microtubule growth speed. Once the stabilizing cap is "lost," the microtubule transitions from growth to shrinkage (Carlier, 1982; Mitchison and Kirschner, 1984). Because the α1B/βI+βIVb microtubules undergo catastrophe less frequently than brain microtubules, we investigated whether there might be a difference in the sizes of their stabilizing GTP caps. The EB1 family of proteins is thought to preferentially bind to the growing microtubule end by sensing the presence of GTP (or GDP-Pi) in the cap structure (Bieling *et al.*, 2007; Kumar and Wittmann, 2012; Maurer *et al.*, 2012). Therefore, it was proposed that the size of the EB1 binding region can be used as a read-out of the GTP cap size (Bieling *et al.*, 2007). We measured EB1-GFP comet lengths at different growth speeds for brain and α1B/βI+βIVb microtubules (Figure 4). The EB1-GFP comet length increases with increasing microtubule growth speed for brain tubulin, as shown in earlier studies (Bieling *et al.*, 2007). This was also observed for α1B/βI+βIVb microtubules (Figure 4, A and B). Interestingly, when brain and α1B/βI+βIVb microtubules are compared at the same growth speeds, the lengths of their EB1-GFP comets are statistically indistinguishable (Figure 4C), suggesting no large differences in their GTP cap sizes. In conclusion, our data indicate that the lower catastrophe frequency and faster growth rates of the α1B/βI+βIVb microtubules that we observe are due mostly to the large differences between the tubulin on-rates at their dynamic ends and not GTP cap sizes. However, we cannot rule out small differences in GTPase rates not detectable in these assays.

### Modulation of α1B/βI+βIVb tubulin dynamics by a neuronal isoform

βIII, a neuronal specific tubulin isoform, is overexpressed in various tumors and has been identified as a strong prognosticator of poor clinical outcomes (Kavallaris, 2010). Its mRNA levels can increase as much as 43- and 71-fold in breast and lung cancers, respectively, when compared with mRNA levels in nontumoral tissues (Leandro-García *et al.*, 2010), and these increases are also manifested in increased βIII protein levels (Hiser *et al.*, 2006). βIII constitutes 25% of tubulin purified from brain tissue (Banerjee *et al.*, 1988) but is not found in any nonneuronal tissue except on transformation (Leandro-García *et al.*, 2010). To understand the effects of neuronal tubulin on microtubule dynamics in nonneuronal cells, we characterized the dynamic parameters of α1B/βI+βIVb tubulin in the presence of increasing amounts of recombinant neuronal α1A/βIII tubulin (Figure 5). We expressed and purified recombinant α1A/βIII tubulin through a double-selection strategy using an affinity-tag on both α- and β-tubulin. This tubulin is >99.9% homogeneous, has no detectable posttranslational modifications, is free of contamination from endogenous insect tubulins, and is assembly competent (Vemu *et al.*, 2016). We titrated recombinant neuronal α1A/βIII tubulin into nonneuronal α1B/βI+βIVb tubulin and measured microtubule dynamics parameters. These show that microtubule dynamic parameters can be tuned by the proportion between these tubulin isotypes (Figure 5 and Supplemental Movie 1). Equimolar amounts of nonneuronal α1B/βI+βIVb and neuronal α1A/βIII results in plus-end growth rates comparable to those of α1A/βIII tubulin alone (Figure 5A) while plus-end catastrophe frequencies are similar to those of neuronal α1A/βIII alone when threefold molar excess of α1A/βIII tubulin is added. α1A/βIII tubulin does not polymerize on its own at the concentrations used; however, we do not know the efficiency of incorporation of the different isoforms into microtubules. At minus ends, α1B/βI+βIVb and α1A/βIII microtubules have very similar growth speeds and only a modest difference in catastrophe frequencies. Interestingly, titration of α1A/βIII does not affect minus-end catastrophe frequency significantly. Our data indicate that α1A/βIII tubulin is incorporated at the minus ends because 1) at 4 μM α1B/βI+βIVb tubulin alone, only ~20% of microtubules exhibit minus-end growth compared with ~60% observed for a combination of 4 μM α1B/βI+βIVb and 2 μM α1A/βIII tubulin, and 2) α1B/βI+βIVb and α1A/βIII tubulin do not polymerize alone at 2 and 4 μM,

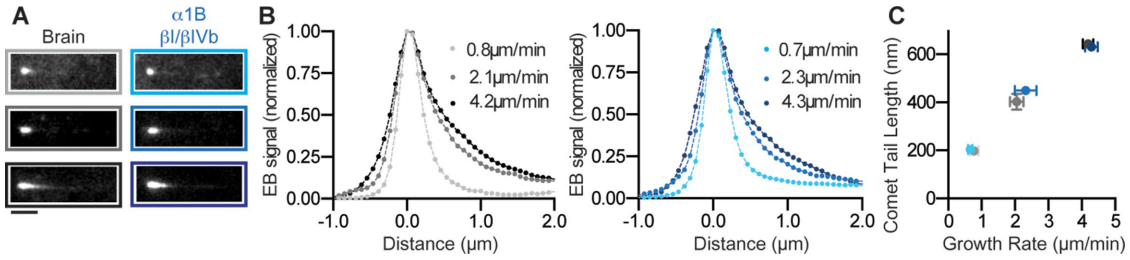


FIGURE 4: EB1-GFP comet analysis on brain and α1B/βI+βIVb microtubules. (A) TIRF microscopy images of EB1-GFP comets at the ends of growing brain microtubules (left) and α1B/βI+βIVb (right) microtubules at different growth speeds. From top to bottom: brain microtubule growth speeds are 0.8, 2.1, and 4.2 μm/min ($n$ = 26, 13, and 15 microtubules, respectively). From top to bottom: α1B/βI+βIVb microtubule growth speeds are 0.7, 2.3, and 4.3 μm/min ($n$ = 24, 12, and 10 microtubules, respectively). Scale bar: 2 μm. (B) Averaged fluorescence intensity profiles of EB1-GFP comets at different growth speeds of brain (left) and α1B/βI+βIVb (right) microtubules. $n$ = 420, 333, and 421 comet profiles from 12, 13, and 15 brain microtubules at growth speeds of 0.8, 2.1, and 4.2 μm/min, respectively and $n$ = 364, 351, and 234 comet profiles for 15, 12, and 10 α1B/βI+βIVb microtubules at growth speeds of 0.7, 2.3, and 4.3 μm/min, respectively. (C) EB1-GFP comet tail lengths as a function of microtubule growth speeds for brain (gray) and α1B/βI+βIVb (blue) microtubules. Comet tail lengths were obtained by single exponential fits to the averaged intensity profiles (see *Materials and Methods*).

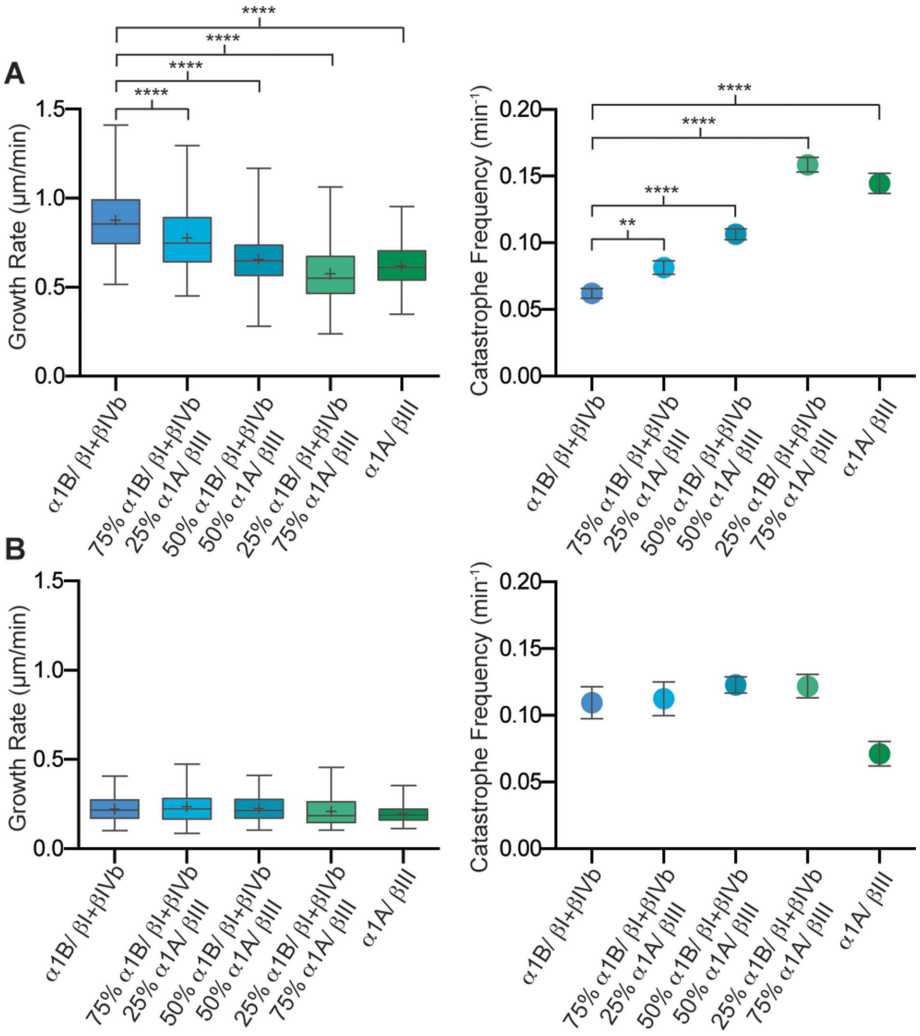


FIGURE 5: Modulation of α1B/βI+βIVb tubulin dynamics by addition of neuronal α1A/βIII tubulin. (A) Left panel: box-whisker plot (whiskers indicate minimum and maximum) showing plus-end growth rates at 6 μM tubulin; $n$ = 191, 258, 432, 377, and 203 events for α1B/βI+βIVb, 75% α1B/βI+βIVb 25% α1A/βIII, 50% α1B/βI+βIVb 50% α1A/βIII, 25% α1B/βI+βIVb 75% α1A/βIII, and α1A/βIII tubulin, respectively. Right panel: plus-end catastrophe frequencies; $n$ = 69, 77, 113, 94, and 85 microtubules for α1B/βI+βIVb, 75% α1B/βI+βIVb 25% α1A/βIII, 50% α1B/βI+βIVb 50% α1A/βIII, 25% α1B/βI+βIVb 75% α1A/βIII, and α1A/βIII tubulin, respectively. ** and ****, $p$ values < 0.01 and < 0.0001, respectively, determined by unpaired $t$ test. (B) Left panel: box-whisker plot (whiskers indicate minimum and maximum) showing minus-end growth rates at 6 μM tubulin; $n$ = 84, 66, 206, 91, and 93 events for α1B/βI+βIVb, 75% α1B/βI+βIVb 25% α1A/βIII, 50% α1B/βI+βIVb 50% α1A/βIII, 25% α1B/βI+βIVb 75% α1A/βIII, and α1A/βIII tubulin, respectively. Right panel: minus-end catastrophe frequencies; $n$ = 33, 34, 59, 30, and 40 microtubules for α1B/βI+βIVb, 75% α1B/βI+βIVb 25% α1A/βIII, 50% α1B/βI+βIVb 50% α1A/βIII, 25% α1B/βI+βIVb 75% α1A/βIII, and α1A/βIII tubulin, respectively.

respectively. The lack of an effect of the α1A/βIII tubulin on minus-end dynamics could be due to either the less-efficient incorporation of this isoform at minus ends than plus ends when compared with α1B/βI+βIVb tubulin or to genuine differences in the effects of α1A/βIII incorporation between minus and plus ends. These experiments also indicate that overexpression of the α1A/βIII tubulin isoform in tumors can significantly alter global microtubule dynamics, with the differences observed being comparable to those elicited by some MAPs such as mitotic centromere-associated kinesin (MCAK) (Walczak *et al.*, 1996), cytoplasmic linker associated proteins (CLASPs) (Al-Bassam *et al.*, 2010), or targeting protein for Xklp2 (TPX2) (Roostalu *et al.*, 2015), but not as dramatic as seen for *Xenopus* microtubule-associated protein 215 (XMAP215) (Brouhard *et al.*, 2008), for example. A destabilizing effect of neuronal βIII tubulin was also observed recently when mixed with recombinant βII tubulin in the presence of an unknown α-tubulin composition that included insect α-tubulin (Pamula *et al.*, 2016), as well as in earlier experiments with brain microtubules depleted of βIII tubulin by immunoaffinity chromatography (Panda *et al.*, 1994).

In conclusion, the majority of in vitro dynamics studies performed use heterogeneous scrambled brain microtubules with isoform composition and posttranslational modifications that are not representative of the many cell types found in our bodies. Recent work showed strikingly different activities of the *S. cerevisiae* tip tracking protein Stu2p on *S. cerevisiae* microtubules compared with heterogeneous brain microtubules (Podolski *et al.*, 2014), demonstrating the importance of studying the effects of regulators with the physiologically relevant tubulin substrate. Our study reports the cryo-EM structure and in vitro dynamics parameters for unmodified α1B/βI+βIVb tubulin purified from a human embryonic kidney cell line with tubulin composition similar to that found in fibroblasts and many cell lines used for cell biological investigations. α1B/βI+βIVb microtubules have dramatically different dynamic parameters than those of brain microtubules characterized by faster growth rates and lower catastrophe frequencies, consistent with the less tapered morphology of their growing ends. Furthermore, we show that the dynamics of these nonneuronal microtubules can be proportionally tuned by the addition of a neuronal tubulin isoform with different dynamic properties. Thus, in addition to the potential isoform specific recruitment of microtubule regulators, different microtubule dynamics in cells can be elicited by modulating the relative expression levels of tubulin isoforms.

## MATERIALS AND METHODS

### Affinity purification of tubulin from brain and tsA201 cells

Tubulin from tsA201 cells was purified as previously described (Widlund *et al.*, 2012; Vemu *et al.*, 2014). Briefly, cells were lysed by gentle sonication in 1XBRB80, pH 6.8 (80 mM piperazine-*N*,*N*′-bis(2-ethanesulfonic acid) [PIPES]), 1 mM $MgCl_2$, 1 mM EGTA), 1 mM dithiothreitol (DTT), and 25 μg/ml benzonase. The lysate was cleared by ultracentrifugation at 444,000 × *g* for 15 min at 4°C. The homogenate was loaded onto an N-hydroxysuccinimide (NHS)-column (GE Healthcare) coupled to TOG1. The tubulin was eluted with 1XBRB80 supplemented with 0.5 M ammonium sulfate and was buffer exchanged using a PD-10 column (GE Healthcare) into 1XBRB80, 10% glycerol, and 20 μM GTP and was flash frozen in liquid nitrogen. The tubulin was further purified by cycling (Castoldi and Popov,

2003). Tubulin was buffer exchanged using a PD10 column into 1XBRB80 and 20μM GTP and flash frozen in liquid nitrogen. Mass spectrometric analysis of this tubulin indicated that it contains one major α-tubulin (α1B) and two β-tubulin (βI+βIVb) isoforms. The same protocol was used to affinity purify tubulin from mouse brains. Wild-type C57/BL6 mice were administered $CO_2$ gas. Their brains were immediately extracted, washed with cold 1XBRB80, pH 6.8, and flash frozen in liquid nitrogen. The brains were thawed on ice and homogenized in 50 mM 2-(*N*-morpholino)ethanesulfonic acid (Mes), pH 6.6, 1 mM $CaCl_2$, 1 mM PMSF, and 1 mM DTT using a polytron three times for 5 s each at low pulses and three times for 5 s at high pulses. The lysate was cleared and tubulin was purified as described above.

### Purification of recombinant single-isoform human tubulin

Recombinant single-isoform human α1A/βIII tubulin was expressed using baculovirus and purified as previously described (Vemu *et al.*, 2016). In brief, α1A with an internal His-tag and βIII with a C-terminal cleavable Flag tag was purified using a Ni-NTA column (Qiagen) and anti-flag G1 affinity resin (Gen Script) to ensure no insect tubulin contamination. The tubulin was further purified by ion exchange chromatography using a Resource Q anion exchange column (GE Healthcare). Peak fractions were combined and buffer exchanged into 1XBRB80 supplemented with 20 μM GTP using a PD10 column.

### In vitro microtubule dynamics assays

GMPCPP-stabilized microtubule seeds were prepared as described in Gell *et al.* (2010). The GMPCPP seeds were immobilized onto neutravidin coated glass as described previously (Szyk *et al.*, 2014). Dynamic assays were performed as described previously (Vemu *et al.*, 2016). The final imaging buffer contained 1XBRB80, pH 6.8, supplemented with 100 mM KCl, 1 mM GTP, 1% pluronic F-127, and oxygen scavengers. An objective heater (Bioptechs) was used to heat the chamber to 30°C. All chambers were sealed and allowed to equilibrate on the microscope stage for 5 min before imaging. Darkfield images were taken once every 5 s. Image acquisition for the determination of accurate depolymerization rates was performed at 40 frames/s. Kymographs were generated from darkfield images using the Multi Kymograph Plugin in ImageJ. Kymographs were hand traced and dynamic parameters were quantified as previously described (Vemu *et al.*, 2016).

### Microtubule cryo-EM sample preparation

α1B/βI+βIVb tubulin was polymerized at 37°C for 45 min at a final concentration of 2.5 mg/ml in BRB80 buffer (80 mM PIPES, 2 mM $MgCl_2$, 1 mM EGTA, 1 mM DTT) with 1 mM GMPCPP. GMPCPP-bound microtubules were double cycled by depolymerizing GMPCPP microtubules on ice for 5 min then repolymerizing at 37°C for 45 min after adding 2 mM GMPCPP. GMPCPP-bound microtubules were diluted to a final concentration of 2.5 μM in BRB20 buffer (20 mM PIPES, 2 mM $MgCl_2$, 1 mM EGTA, 1 mM DTT) and added to glow-discharged C-flat holey carbon grids (Protochips, 2 μm holes, 4 μm spacing). Human kinesin-3 motor domain (20 μM; Kif1A, residues 1–361, see Atherton *et al.* [2014]) in BRB20 containing 2 mM 5′ adenylyl-β,γ-imidodiphosphate (AMPPNP) was applied to the grid, and the sample was blotted and then vitrified in liquid ethane using a Vitrobot (FEI Co.) operating at 25°C and 100% humidity.

Dynamic microtubules were prepared by polymerizing 5 mg/ml α1B/βI+βIVb, bovine brain tubulin (Cytoskeleton) or mouse brain tubulin (TOG-affinity purified) in BRB80 buffer with 1 mM GTP at 37°C for 2 min. The sample was applied to holey carbon grids in a Vitrobot (FEI Co.) operating at 37°C and 70% humidity and allowed to polymerize for a further minute before blotting and vitrification in liquid ethane.

### Data collection and subframe processing for three-dimensional reconstruction

Images of microtubule-kinesin complexes were collected on a FEI Tecnai G2 Polara operating at 300 kV with a DE20 direct electron detector (Direct Electron) with a calibrated magnification of 52,117× corresponding to a final sampling of 1.22 Å/pixel and a defocus range of 0.5–3.5 μm. A total electron dose of ~50e-/Å$^2$ over a 1.5 s exposure and a frame rate of 15 frames/s was used, giving in a total of 23 frames at ~2.2e-/Å$^2$/frame. Subframe processing was performed as described previously (Vemu *et al.*, 2016). In brief, individual ~2.2e-/Å$^2$ frames were globally aligned using Imod scripts (Kremer *et al.*, 1996) and then locally aligned using the Optical Flow approach (Abrishami *et al.*, 2015) implemented in Xmipp (de la Rosa-Trevin *et al.*, 2013). The full dose of ~50e-/Å$^2$ was used for particle picking and CTF determination in CTFFind3 (Mindell and Grigorieff, 2003), and ~25e-/Å$^2$ was used in particle processing to center particles and determine their Euler angles.

### Cryo-EM data processing

Data processing was performed as previously described (Vemu *et al.*, 2016). Briefly, straight kinesin-3–decorated 14pf microtubules were manually boxed in Eman Boxer, serving as input for a set of custom-designed semi-automated single-particle processing scripts utilizing Spider and Frealign as described previously (Sindelar and Downing, 2007) with minor modifications. The final 14pf microtubule reconstruction was assessed for overfitting during refinement using a high-resolution noise-substitution test (Chen *et al.*, 2013). Using local resolution estimates determined with the *blocres* program in Bsoft, the reconstruction was sharpened with a Bfactor of −180 up to a resolution of 5.5 or 4 Å for visualization of kinesin or tubulin densities respectively.

### Cryo-EM model building and refinement

α1B/βI tubulin was built directly into density in Coot (Emsley *et al.*, 2010) using the recently solved high-resolution cryo-EM model of the brain tubulin 14pf GMPCPP microtubule (PDB 3JAT [Zhang *et al.*, 2015]) as a starting model. After model building, real-space refinement with symmetry restraints was performed in Phenix followed by refinement with symmetry restraints in REFMAC v5.8 modified for cryo-EM data (Supplemental Table 1) (Brown *et al.*, 2015). Secondary structure and reference restraints used with REFMAC based on the high-resolution tubulin crystal structure PDB 4DRX (Pecqueur *et al.*, 2012) were generated with ProSMART (Nicholls *et al.*, 2012).

### Protofilament number, ring, and end-length quantification

Using a FEI Tecnai T12 operating at 120 kV and a 4kx4k charge-coupled device (CCD) camera (Gatan) images of dynamic brain or α1B/βI+βIVb tubulin microtubules were collected. A defocus range of 2–4 μm, a total dose of 30e- over a 1 s exposure, and low pass/Fourier filtering was used to allow visualization of moiré patterns and thereby assign the microtubule protofilament and helical start number (Ray *et al.*, 1993). Ring diameters in these dynamic samples were quantified only for closed single rings using straight line and "measure" in FIJI (Schindelin *et al.*, 2012) from the longest edge-to-edge distance in rings imaged at different projection angles. The axial length of curved end regions in dynamic microtubule preparations were also measured using straight line and "measure" in FIJI by drawing a straight line continuing along the microtubule axis

from the start of the curved/tapered region to the microtubule extreme end.

### EB1-GFP tip tracking

Human full-length EB1 fused to a C-terminal GFP-tag was purified using a Ni-affinity column. The final concentration of EB1 in the experiments was 100 nM. Comets were analyzed to determine the average decay length of the GFP signal on the microtubule. First, ImageJ was used to draw kymographs of growing microtubule tips. These kymographs were then read by a custom-written MATLAB (Mathworks) script. First, the maximum intensity in each line was found and a Gaussian fit to the line profile covering 3 µm of the lattice and extending 2 µm beyond the microtubule tip was performed to find the center of the comet. The location of the center was then subtracted from each data point such that the brightest part of the tip is located at the origin. These steps were repeated for each line in the kymograph. Next, all of the aligned comet profiles were binned into single pixel size bins (77 nm), and their average values were calculated. These data were then plotted in Prism and fitted to a single exponential from the first pixel after the peak to the end of the comet tail. The mean decay length for each comet was determined from the inverse of the exponential decay constant. For all exponential fits, $R^2 > 0.99$.

### Accession numbers

The PDB and EMDB accession codes for the GMPCPP α1B/βI+βIVb microtubule reconstruction are 5N5N and 3589, respectively, and will be released after publication.

## ACKNOWLEDGMENTS

J.A. and C.A.M. are supported by the Medical Research Council, UK (MR/J000973/1). A.V., J.O.S., and A.R.-M. are supported by the Intramural Programs of the National Institute of Neurological Disorders and Stroke and the National Heart, Lung and Blood Institute, National Institutes of Health.

## REFERENCES

Abrishami V, Vargas J, Li X, Cheng Y, Marabini R, Sorzano CO, Carazo JM (2015). Alignment of direct detection device micrographs using a robust optical flow approach. J Struct Biol 189, 163–176.

Al-Bassam J, Kim H, Brouhard G, van Oijen A, Harrison SC, Chang F (2010). CLASP promotes microtubule rescue by recruiting tubulin dimers to the microtubule. Dev Cell 19, 245–258.

Alushin GM, Lander GC, Kellogg EH, Zhang R, Baker D, Nogales E (2014). High-resolution microtubule structures reveal the structural transitions in αβ-tubulin upon GTP hydrolysis. Cell 157, 1117–1129.

Atherton J, Farabella I, Yu IM, Rosenfeld SS, Houdusse A, Topf M, Moores CA (2014). Conserved mechanisms of microtubule-stimulated ADP release, ATP binding, and force generation in transport kinesins. Elife 3, e03680.

Banerjee A, Roach M, Wall K, Lopata M, Cleveland D, Luduena R (1988). A monoclonal antibody against the type II isotype of beta-tubulin. Preparation of isotypically altered tubulin. J Biol Chem 263, 3029–3034.

Bieling P, Laan L, Schek H, Munteanu EL, Sandblad L, Dogterom M, Brunner D, Surrey T (2007). Reconstitution of a microtubule plus-end tracking system in vitro. Nature 450, 1100–1105.

Brouhard GJ, Stear JH, Noetzel TL, Al-Bassam J, Kinoshita K, Harrison SC, Howard J, Hyman AA (2008). XMAP215 is a processive microtubule polymerase. Cell 132, 79–88.

Brown A, Long F, Nicholls RA, Toots J, Emsley P, Murshudov G (2015). Tools for macromolecular model building and refinement into electron cryo-microscopy reconstructions. Acta Crystallogr D Biol Crystallogr 71, 136–153.

Carlier M-F (1982). Guanosine-5′-triphosphate hydrolysis and tubulin polymerization. Mol Cell Biochem 47, 97–113.

Castoldi M, Popov AV (2003). Purification of brain tubulin through two cycles of polymerization–depolymerization in a high-molarity buffer. Protein Expression Purif 32, 83–88.

Chen S, McMullan G, Faruqi AR, Murshudov GN, Short JM, Scheres SH, Henderson R (2013). High-resolution noise substitution to measure overfitting and validate resolution in 3D structure determination by single particle electron cryomicroscopy. Ultramicroscopy 135, 24–35.

Chrétien D, Fuller SD, Karsenti E (1995). Structure of growing microtubule ends: two-dimensional sheets close into tubes at variable rates. J Cell Biol 129, 1311–1328.

de la Rosa-Trevin JM, Oton J, Marabini R, Zaldivar A, Vargas J, Carazo JM, Sorzano CO (2013). Xmipp 3.0: an improved software suite for image processing in electron microscopy. J Struct Biol 184, 321–328.

Denoulet P, Eddé B, Gros F (1986). Differential expression of several neuro-specific β-tubulin mRNAs in the mouse brain during development. Gene 50, 289–297.

Emsley P, Lohkamp B, Scott WG, Cowtan K (2010). Features and development of Coot. Acta Crystallogr D Biol Crystallogr 66, 486–501.

Garnham CP, Vemu A, Wilson-Kubalek EM, Yu I, Szyk A, Lander GC, Milligan RA, Roll-Mecak A (2015). Multivalent microtubule recognition by tubulin tyrosine ligase-like family glutamylases. Cell 161, 1112–1123.

Gell C, Bormuth V, Brouhard GJ, Cohen DN, Diez S, Friel CT, Helenius J, Nitzsche B, Petzold H, Ribbe J, *et al.* (2010). Microtubule dynamics reconstituted in vitro and image by single-molecule fluorescence microscopy. Methods Cell Biol 95, 221–245.

Grishchuk EL, Molodtsov MI, Ataullakhanov FI, McIntosh JR (2005). Force production by disassembling microtubules. Nature 438, 384–388.

Hiser L, Aggarwal A, Young R, Frankfurter A, Spano A, Correia JJ, Lobert S (2006). Comparison of beta-tubulin mRNA and protein levels in 12 human cancer cell lines. Cell Motil Cytoskeleton 63, 41–52.

Horio TH, Hotani H (1986). Visualization of the dynamic instability of individual microtubules by dark-field microscopy. Nature 321, 605–607.

Hoyle HD, Raff EC (1990). Two Drosophila beta tubulin isoforms are not functionally equivalent. J Cell Biol 111, 1009–1026.

Kavallaris M (2010). Microtubules and resistance to tubulin-binding agents. Nat Rev Cancer 10, 194–204.

Kremer JR, Mastronarde DN, McIntosh JR (1996). Computer visualization of three-dimensional image data using IMOD. J Struct Biol 116, 71–76.

Kumar P, Wittmann T (2012). +TIPs: SxIPping along microtubule ends. Trends Cell Biol 22, 418–428.

Leandro-García LJ, Leskelä S, Landa I, Montero-Conde C, López-Jiménez E, Letón R, Cascón A, Robledo M, Rodríguez-Antona C (2010). Tumoral and tissue-specific expression of the major human β-tubulin isotypes. Cytoskeleton 67, 214–223.

Lopata MA, Cleveland DW (1987). In vivo microtubules are copolymers of available beta-tubulin isotypes: localization of each of six vertebrate beta-tubulin isotypes using polyclonal antibodies elicited by synthetic peptide antigens. J Cell Biol 105, 1707–1720.

Mandelkow EM, Mandelkow E, Milligan RA (1991). Microtubule dynamics and microtubule caps: a time-resolved cryo-electron microscopy study. J Cell Biol 114, 977–991.

Maurer SP, Fourniol FJ, Bohner G, Moores CA, Surrey T (2012). EBs recognize a nucleotide-dependent structural cap at growing microtubule ends. Cell 149, 371–382.

Mindell JA, Grigorieff N (2003). Accurate determination of local defocus and specimen tilt in electron microscopy. J Struct Biol 142, 334–347.

Minoura I, Hachikubo Y, Yamakita Y, Takazaki H, Ayukawa R, Uchimura S, Muto E (2013). Overexpression, purification, and functional analysis of recombinant human tubulin dimer. FEBS Lett 587, 3450–3455.

Mitchison TK, Kirschner M (1984). Dynamic instability of microtubule growth. Nature 312, 237–242.

Murphy DB, Wallis KT (1983). Isolation of microtubule protein from chicken erythrocytes and determination of the critical concentration for tubulin polymerization in vitro and in vivo. J Biol Chem 258, 8357–8364.

Murphy DB, Wallis KT (1986). Erythrocyte microtubule assembly in vitro. Tubulin oligomers limit the rate of microtubule self-assembly. J Biol Chem 261, 2319–2324.

Newton CN, DeLuca JG, Himes RH, Miller HP, Jordan MA, Wilson L (2002). Intrinsically slow dynamic instability of HeLa cell microtubules in vitro. J Biol Chem 277, 42456–42462.

Nicholls RA, Long F, Murshudov GN (2012). Low-resolution refinement tools in REFMAC5. Acta Crystallogr D Biol Crystallogr 68, 404–417.

Pamula MC, Ti S-C, Kapoor TM (2016). The structured core of human β tubulin confers isotype-specific polymerization properties. J Cell Biol 213, 425–433.

Panda D, Miller HP, Banergee A, Ludena RF, Wilson L (1994). Microtubule dynamics in vitro are regulated by the tubulin isotype composition. Proc Natl Acad Sci USA 91, 11358–11362.

Pecqueur L, Duellberg C, Dreier B, Jiang Q, Wang C, Pluckthun A, Surrey T, Gigant B, Knossow M (2012). A designed ankyrin repeat protein selected to bind to tubulin caps the microtubule plus end. Proc Natl Acad Sci USA 109, 12011–12016.

Podolski M, Mahamdeh M, Howard J (2014). Stu2, the budding yeast XMAP215/Dis1 homolog, promotes assembly of yeast microtubules by increasing growth rate and decreasing catastrophe frequency. J Biol Chem 289, 28087–28093.

Rao S, Aberg F, Nieves E, Band Horwitz S, Orr GA (2001). Identification by mass spectrometry of a new alpha-tubulin isotype expressed in human breast and lung carcinoma cell lines. Biochemistry 40, 2096–2103.

Ray S, Meyhofer E, Milligan RA, Howard J (1993). Kinesin follows the microtubule's protofilament axis. J Cell Biol 121, 1083–1093.

Redeker V (2010). Mass spectrometry analysis of C-terminal posttranslational modifications of tubulins. Methods Cell Biol 95, 77–103.

Rice LM, Montabana EA, Agard DA (2008). The lattice as allosteric effector: structural studies of alphabeta- and gamma-tubulin clarify the role of GTP in microtubule assembly. Proc Natl Acad Sci USA 105, 5378–5383.

Roostalu J, Cade NI, Surrey T (2015). Complementary activities of TPX2 and chTOG constitute an efficient importin-regulated microtubule nucleation module. Nat Cell Biol 17, 1422–1434.

Saillour Y, Broix L, Bruel-Jungerman E, Lebrun N, Muraca G, Rucci J, Poirier K, Belvindrah R, Francis F, Chelly J (2014). Beta tubulin isoforms are not interchangeable for rescuing impaired radial migration due to Tubb3 knockdown. Hum Mol Genet 23, 1516–1526.

Schindelin J, Arganda-Carreras I, Frise E, Kaynig V, Longair M, Pietzsch T, Preibisch S, Rueden C, Saalfeld S, Schmid B, *et al*. (2012). Fiji: an open-source platform for biological-image analysis. Nat Methods 9, 676–682.

Sindelar CV, Downing KH (2007). The beginning of kinesin's force-generating cycle visualized at 9-A resolution. J Cell Biol 177, 377–385.

Szyk A, Deaconescu AM, Spector J, Goodman B, Valenstein ML, Ziolkowska NE, Kormendi V, Grigorieff N, Roll-Mecak A (2014). Molecular basis for age-dependent microtubule acetylation by tubulin acetyltransferase. Cell 157, 1405–1415.

VanBuren V, Odde DJ, Cassimeris L (2002). Estimates of lateral and longitudinal bond energies within the microtubule lattice. Proc Natl Acad Sci USA 99, 6035–6040.

Vemu A, Atherton J, Spector JO, Szyk A, Moores CA, Roll-Mecak A (2016). Structure and dynamics of single-isoform recombinant neuronal human tubulin. J Biol Chem 291, 12907–12915.

Vemu A, Garnham CP, Lee D-Y, Roll-Mecak A (2014). Generation of differentially modified microtubules using in vitro enzymatic approaches. Methods Enzymol 540, 149–166.

Villasante A, Wang D, Dobner P, Dolph P, Lewis S, Cowan N (1986). Six mouse alpha-tubulin mRNAs encode five distinct isotypes: testis-specific expression of two sister genes. Mol Cell Biol 6, 2409–2419.

Walczak CE, Mitchison TJ, Desai A (1996). XKCM1: a Xenopus kinesin-related protein that regulates microtubule dynamics during mitotic spindle assembly. Cell 84, 37–47.

Wang D, Villasante A, Lewis SA, Cowan NJ (1986). The mammalian beta-tubulin repertoire: hematopoietic expression of a novel, heterologous beta-tubulin isotype. J Cell Biol 103, 1903–1910.

Wang HW, Nogales E (2005). Nucleotide-dependent bending flexibility of tubulin regulates microtubule assembly. Nature 435, 911–915.

Weisenberg RC, Broisy GG, Taylor EW (1968). Colchicine-binding protein of mammalian brain and its relation to microtubules. Biochemistry 7, 4466–4479.

Widlund PO, Podolski M, Reber S, Alper J, Storch M, Hyman AA, Howard J, Drechsel DN (2012). One-step purification of assembly-competent tubulin from diverse eukaryotic sources. Mol Biol Cell 23, 4393–4401.

Yu I, Garnham CP, Roll-Mecak A (2015). Writing and reading the tubulin code. J Biol Chem 290, 17163–17172.

Zambito AM, Knipling L, Wolff J (2002). Charge variants of tubulin, tubulin S, membrane-bound and palmitoylated tubulin from brain and pheochromocytoma cells. Biochim Biophys Acta 1601, 200–207.

Zhang R, Alushin GM, Brown A, Nogales E (2015). Mechanistic origin of microtubule dynamic instability and its modulation by EB proteins. Cell 162, 849–859.

# Supplemental Materials

***Molecular Biology of the Cell***

Vemu et al.

**Supplementary Figures**

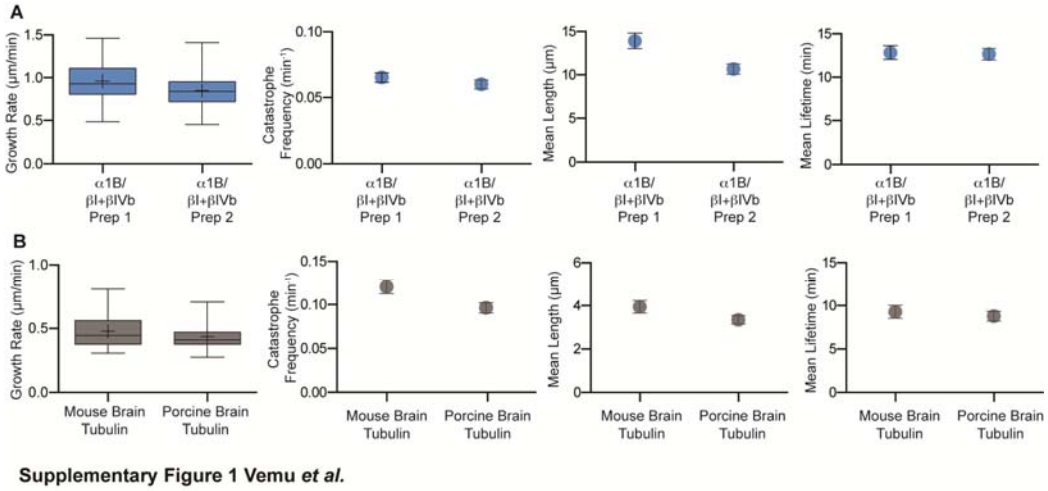


**Supplementary Figure 1 Vemu *et al.***

**Supplementary Figure 1.**Consistent dynamic parameters for α1B/βI+βIVband brain tubulin from different purifications.**(A)** Consistent dynamic parameters for α1B/βI+βIVbtubulin from different purifications. *From left to right:* Box-whisker plot (whiskers indicate minimum and maximum) showing plus-end growth rates at 6μM tubulin from two different tubulin preparations; n= 246 and 191 events for purification 1 and purification 2, respectively. Plus-end catastrophe frequencies; n = 90 and 69 microtubules. Plus-end microtubule lengths; n = 74 and 102 events. Plus-end microtubule lifetimes; n = 74 and 102 eventsfor purification 1 and purification 2, respectively. (B). Dynamic parameters of mouse brain tubulin purified *via* the TOG affinity approach and commercial brain tubulin (Cytoskeleton Inc.). *From left to right:* Box-whisker plot (whiskers indicate minimum and maximum) showing plus-end growth rates at 6μM □tubulin□□from the two different tubulin preparations; n= 38 and 101 events for mouse brain tubulin and commercial porcine tubulin, respectively. Plus-end catastrophe frequencies; n = 20 and 32 microtubules. Plus-end microtubule

lengths; n = 49 and 76 events. Plus-end microtubule lifetimes; n = 49 and 76 eventsfor mouse brain tubulin and commercial tubulin, respectively.

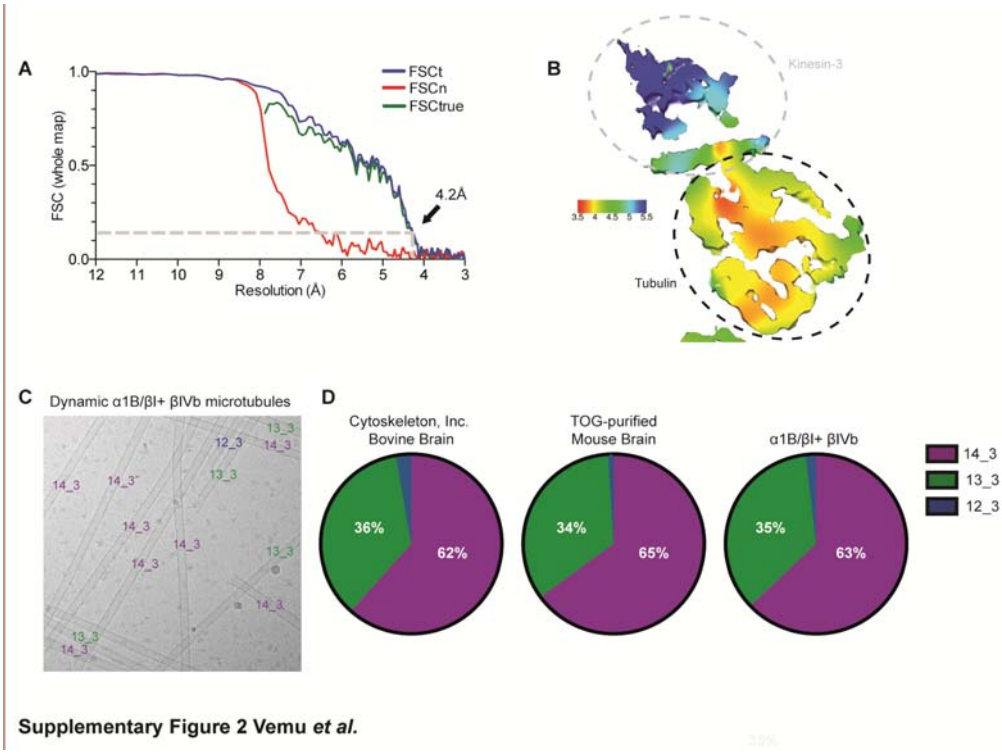


**Supplementary Figure 2.**Resolution estimates and protofilament number analysis forα1B/βI+βIVb microtubules.(A) Utilizing the gold-standard noise substitution method(Chen *et al.*, 2013)the $FSC_{true}$ curve gives an overall resolution estimate of 4.2Å for the reconstruction ofα1B/βI+βIVb GMPCPP microtubules bound to kinesin-3. (B) Using the Bsoft program blocres(Cardone *et al.*, 2013) local resolution estimates were calculated and used to color the unfiltered whole reconstruction density. Red density corresponds to 3.5 Å resolution, with a continuum of colors indicating the resolution gradient, ending with blue at 5.5 Å resolution. Tubulin is at a higher resolution, ranging from ~3.5 Å in central regions to ~4.5 Å in more flexible peripheral surface-exposed regions. Kinesin-3, used as a fiducial marker for alignment purposes, is at lower

resolution (resolution of ~5.5 Å) and is excluded from display items. (C) Raw image of dynamic$\alpha$1B/$\beta$I+$\beta$IVb microtubules. Microtubules are individually labeled with their protofilament number (from 12-14) and start number (3) according to analysis of their Moire patterns(Wade *et al.*, 1990). (D) Quantification of protofilament number distributions for dynamic brain (mouse tubulin purified *via* the TOG approach or commercial bovine brain tubulin (Cytoskeleton Inc.)) or $\alpha$1B/$\beta$I+$\beta$IVb microtubules polymerized under identical conditions.n = 73, 200 and 108 microtubules for bovine brain, mouse brain, and $\alpha$1B/$\beta$1+$\beta$IVb, respectively.

**Supplementary Table 1: Refinement statistics and modelgeometry**

| | |
|---|---|
| Resolution for refinement (Å) | 4.2 |
| Map sharpening Bfactor (Å$^2$) | -180 |
| $FSC_{average}$[a] | 0.72 |
| Rms deviations (bonds)(Å$^2$) | 0.007 |
| Rms deviations (angles)(Å$^2$) | 1.135 |
| Molprobity Score | 1.07 (100$^{th}$ percentile) |
| Clashscore, all atoms | 1.36 (100th percentile) |
| Poor rotamers (%) | 0.14% |
| Ramachandran plot favoured (%) | 96.70% |
| Ramachandran outliers (%) | 0.24% |

[a]FSCaverage = $\Sigma(N_{shell}FSC_{shell})/\Sigma(N_{shell})$, where $FSC_{shell}$ is the FSC in a given shell, $N_{shell}$ is the number of structural factors in the shell. $FSC_{shell} = \Sigma(F_{model}\ F_{EM})/(\sqrt{\ }\Sigma\ (|F|2_{model}))\sqrt{\ }\Sigma\ (F^2_{EM}))$